Cell Reports
Physical Science

CellPress
OPEN ACCESS

Article

Short- and long-range crowding effects on water's hydrogen bond networks

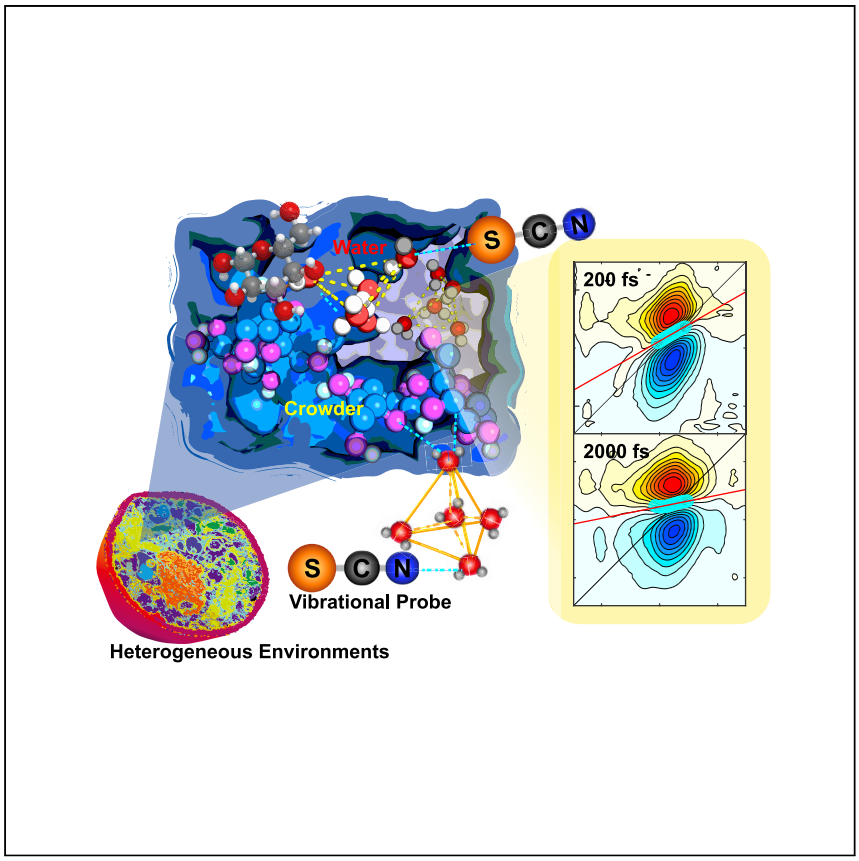

Cells contain high concentrations of biomolecules, including lipids, proteins, and osmolytes, which shape the cytoplasm. Therefore, intracellular water is highly confined. Confinement gives intracellular water unique properties that determine the stability, structure, and dynamics of proteins within these environments. However, the complex molecular effects of crowding are often overlooked. You et al. quantitatively define crowded environments by studying the tetrahedral structure and H-bond dynamics of water. They demonstrate that crowders impart different short- and long-range order on water.

Xiao You, Joseph C. Shirley, Euihyun Lee, Carlos R. Baiz

xiao.you@austin.utexas.edu (X.Y.)
cbaiz@cm.utexas.edu (C.R.B.)

Highlights

Molecular crowding in cytoplasmic environments produces heterogeneous environments

Crowder-water H-bond interactions drive dynamics within local environments

Short-range crowding effects introduce increased hydrogen bond disorder

Long-range crowding effects stabilize ice-like tetrahedral hydrogen bond networks

You et al., Cell Reports Physical Science 2, 100419
May 19, 2021
https://doi.org/10.1016/j.xcrp.2021.100419

Please cite this article in press as: You et al., Short- and long-range crowding effects on water's hydrogen bond networks, Cell Reports Physical Science (2021), https://doi.org/10.1016/j.xcrp.2021.100419

Cell Reports
Physical Science

CellPress
OPEN ACCESS

Article

Short- and long-range crowding effects on water's hydrogen bond networks

Xiao You,[1,*] Joseph C. Shirley,[1] Euihyun Lee,[1] and Carlos R. Baiz[1,2,*]

SUMMARY

Intracellular water is highly confined with approximately 40% of the cell volume occupied by biomolecules. Crowding alters water dynamics and interactions with biomolecules. In biochemical experiments, artificial crowders are commonly used to mimic intracellular environments, but their effects on biomolecules remain elusive. Here, we investigate the crowding effects by directly accessing the picosecond hydrogen-bond dynamics in crowded solutions using ultrafast two-dimensional infrared spectroscopy and all-atom molecular dynamics simulations. We quantify the effects of different crowding agents: small sugars; polysaccharides; and polyethylene glycol (PEG). Our results show that crowders introduce disorder within the first two solvation shells but stabilize ice-like order in water >1 nm from the crowder. The results show that accounting for crowder chemical structure, conformation, and crowder-solvent interactions is a key step toward a complete description of crowded solutions for *in vitro* for biomolecular studies.

INTRODUCTION

Water is an essential participant in all biochemical processes. Compared to pure water, intercellular water is strongly confined by biomolecules,[1] including proteins, nucleic acids, osmolytes, ions, and sugars; these components constitute up to ~40% of the cytoplasmic volume.[2,3] Crowding modulates protein stability through direct interactions with biomolecules or indirect modulation of the intracellular environment.[4,5] Indeed, intracellular water generally exhibits slower H-bond dynamics than bulk water.[6]

Water's H-bond networks are arguably the most important determinant of biomolecular structure, dynamics, stability, and function.[7,8] Indeed, proteins are slaved to the motions of the solvent.[9] However, confinement effects on H-bond network restructuring dynamics remain underexplored. Disrupted H-bond networks are generally associated with slower H-bond dynamics, as a result of an imbalance between donors and acceptors.[10,11] The influence of crowders on water likely depends not only on its concentration but also on its chemical properties.[12] The specific relationship between crowder composition and water H-bond networks has not been fully established. Characterizing these interdependent relations in crowded solutions is therefore an important first step toward determining the ability of crowders to mimic the cytosol.

Significant efforts have been focused on quantifying crowding effects on biomolecules,[13–16] including protein stability and protein-protein interactions.[4,7,11,17] Traditionally, crowding has been defined as a balance of two types of interactions: (1) hard-core repulsions and (2) weak intermolecular interactions. Hard-core repulsions,

[1]Department of Chemistry, University of Texas at Austin, Austin, TX 78757, USA

[2]Lead contact

*Correspondence:
xiao.you@austin.utexas.edu (X.Y.),
cbaiz@cm.utexas.edu (C.R.B.)

https://doi.org/10.1016/j.xcrp.2021.100419

Please cite this article in press as: You et al., Short- and long-range crowding effects on water's hydrogen bond networks, Cell Reports Physical Science (2021), https://doi.org/10.1016/j.xcrp.2021.100419

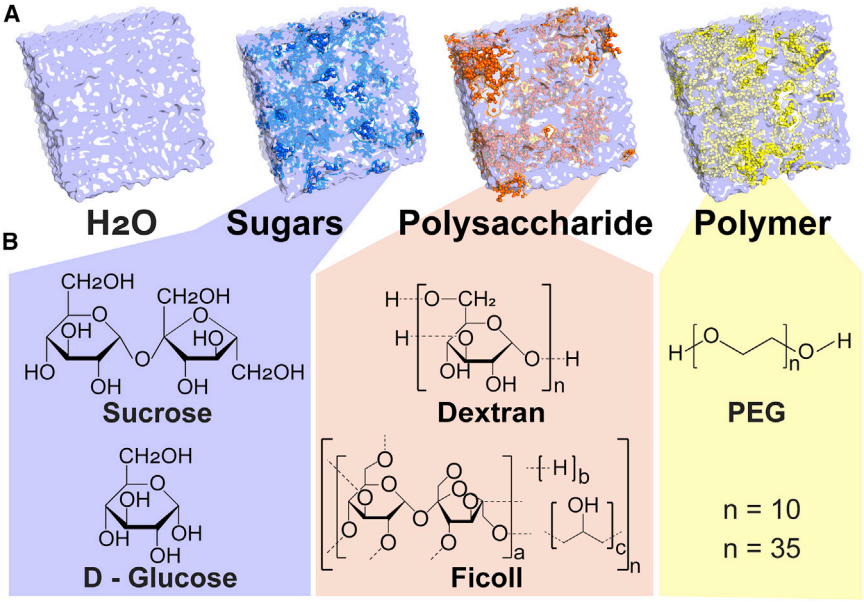

Figure 1. Illustration of the crowded aqueous environments

(A) Snapshots of the molecular dynamics simulation boxes for three different types of crowders: mono- and disaccharides (glucose and sucrose), polysaccharides (dextran and Ficoll), and polymers (PEG); see Experimental procedures section for details.

(B) Molecular structures of the crowding agents.

or excluded volume effects, are non-specific interactions that stabilize compact structures with low surface-area-to-volume ratios as a result of loss in configurational entropy.[4] Excluded volume contributions depend on concentration and crowder size, but not on its chemical properties. Recently, it has become evident that excluded volume alone is insufficient to describe crowding effects.[18] Even within "inert" polymers, backbone-water interactions perturb the H-bond networks beyond the first solvation shell.[19] Enthalpy-driven, non-specific interactions can both stabilize or destabilize native structures depending on the specific molecular makeup of the crowder and, as such, are significantly more difficult to characterize.[16,20–22]

Here, we characterize non-specific crowder interactions by exploring the water H-bond network structure and dynamics using crowding agents, including sugars and polyethylene glycol (PEG). Our combined experimental and simulation studies explore short- and long-range crowder effects on the tetrahedral H-bond networks. Interestingly, our findings indicate that crowders decrease the tetrahedral H-bond ordering near the crowder interface while increasing tetrahedral ordering within the solution for water distant from crowder interfaces.

RESULTS AND DISCUSSION

Complex H-bond network in crowded solutions

Intracellular biomolecule concentrations can reach 400 mg/mL or as much as 40% of the cytosolic volume.[2] Saccharides and PEG are most commonly used as crowding agents in biochemical studies due to their excellent solubility and biocompatibility.[23] Here, we investigate three types of crowders: mono- and disaccharides, linear and branched polysaccharides, as well as PEG with two different molecular sizes (M_w = 600 and 1,500), which correspond to approximately 10 mer and 35 mer (Figure 1). Solute concentrations of 400 mg/mL of H_2O (28% by mass) solvent were used to explore the concentration range relevant to intracellular environments.

Please cite this article in press as: You et al., Short- and long-range crowding effects on water's hydrogen bond networks, Cell Reports Physical Science (2021), https://doi.org/10.1016/j.xcrp.2021.100419

Mono- and disaccharides support strong H-bond interactions with water as a result of the large number of hydroxyl groups. These OH groups donate as well as accept H-bonds, largely maintaining the donor-acceptor balance. The interactions between polysaccharides and water, on the other hand, depend strongly on the size and branching ratio of the polymer. For example, the flexible and linear polysaccharide dextran and the highly branched Ficoll affect protein conformation differently. The branched structure leads to more significant polymer self-interactions compared to dextran.[5] The effects of crowder self-interactions and their role in reshaping the solvent H-bond networks remain difficult to disentangle. PEG only accepts H-bonds through its ether oxygens,[24] but importantly, the PEG backbone is solvated by ordered waters, due to the polarity of its oxygen atoms, explaining PEG's high solubility and biocompatibility.[24,25] Density, viscosity, and water activity in PEG solutions are influenced by both the concentration and molecular mass of the polymer,[26,27] though ultrafast dynamics are largely independent of polymer length, suggesting that "bulk" properties are not a useful measure of local H-bond rearrangements in these solutions.[25] Considering the structural differences between crowders, this work presents a direct comparison of the local and bulk H-bond structure and dynamics across crowders.

MD simulation shows heterogeneous H-bond network structure in crowded solutions

The Experimental procedures section describes the MD simulation procedure. Each trajectory was analyzed to quantify the H-bond network structure, which is described through the tetrahedral order parameter, q. This parameter measures the projection of a water molecule's H-bond geometry onto a perfect tetrahedron.[28,29] Quantitatively, q is defined as[29,30]

$$q = 1 - \frac{3}{8}\sum_{j=1}^{3}\sum_{k=j+1}^{4}\left(\cos\left(\psi_{jk}\right) + \frac{1}{3}\right)^2, \qquad \text{(Equation 1)}$$

where ψ_{jk} represents the angle formed by the central water oxygen atom with each pair of its nearest neighbors (illustration in Figure 2A). In hexagonal ice, all the angles are 109.5°, giving the parameter a value of $q = 1$. In an ideal gas, random positions and orientations result in a value of $\langle q \rangle = 0$.[31]

Figure 2A shows the order parameter, q, distributions across crowders. The bimodal distribution, showing a high-q peak around $q = 0.8$ and a low-q peak around $q = 0.45$, is interpreted as populations of predominantly structured or unstructured water, respectively.[29] The lower peak has a higher amplitude in the crowded solutions compared to pure water. This low-q peak is interpreted as water with partially disrupted H-bond networks. In comparison with pure water (red curve), crowders increase the amplitude of the low-q peak, which means that crowding increases the fraction of unstructured water. Among the selected crowders, glucose and sucrose exhibit higher amplitudes of the disordered peak, suggesting that mono- and disaccharides lead to larger "unstructured water" populations compared to Ficoll, dextran, or PEG. However, considering that crowders exhibit different amounts of interfacial and bulk water, it is important to further examine these contributions toward the order parameter distributions.

The sugar hydroxyl groups allow for direct H-bonding with water molecules, as shown by the 0.2-nm peak in the water-to-crowder distance histograms (Figure 2B), suggesting that the OH groups may perturb the local H-bond networks in these crowders. Although PEG can also form direct H-bonds with water, there is a greater

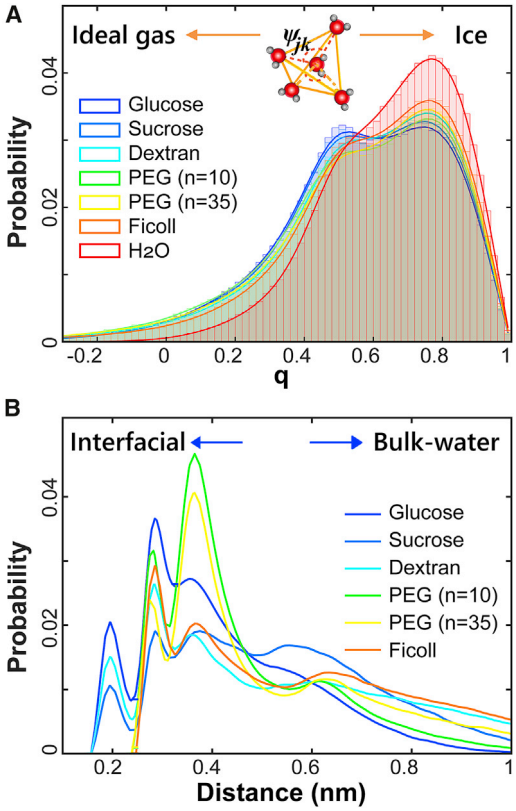

Figure 2. Tetrahedral order parameter and water-crowder distance

(A) Tetrahedral order parameter distributions (Equation 1) for the different crowders extracted from MD simulations. The bimodal distributions exhibit two peaks centered around $q = 0.45$ and $q = 0.8$ assigned to structured and unstructured water, respectively.

(B) Distribution of water-crowder distances. Sugars contain a higher proportion of interfacial water as a result of their higher surface area compared to polymer solutions, where a larger proportion of water is located further away from the crowder. The distributions are calculated by computing the distances from all water atoms, including hydrogens, to the nearest crowder atom.

number of water molecules at intermediate distances to PEG (~0.4 nm), indicating that water has fewer direct interactions with the PEG backbone. This suggests that PEG forms "crowder-rich" clusters, which may explain the fast water dynamics observed in PEG, as will be discussed later in the article.

Analysis of the order parameter as a function of the distance between the central water and the crowder provides insight into the short- and long-distance effects of the crowders (Figure 3). Interfacial waters may have incomplete or disrupted solvation shells (<0.35 nm from the crowder) and therefore exhibit a lower q value, as the average O–O distance in pure water is approximately 0.3 nm.[32] Interestingly, the first solvation shell waters in the glucose and sucrose solutions exhibit less disrupted H-bond networks compared to polymers. The q values are higher for sucrose and glucose compared to PEG, suggesting that the large number of hydroxyl groups in sugars partially stabilizes "bulk-like" tetrahedral H-bond networks within the first few solvation shells. This can be interpreted as follows: PEG adopts compact conformations in water,[33,34] thus being characterized by a weaker tendency to form H-bonds with water, and therefore, water adjacent to PEG also becomes less ordered compared to sucrose/glucose, which leads to lower q values for interfacial water in PEG (Figure 3). The two polysaccharides, Ficoll, and dextran, behave

Please cite this article in press as: You et al., Short- and long-range crowding effects on water's hydrogen bond networks, Cell Reports Physical Science (2021), https://doi.org/10.1016/j.xcrp.2021.100419

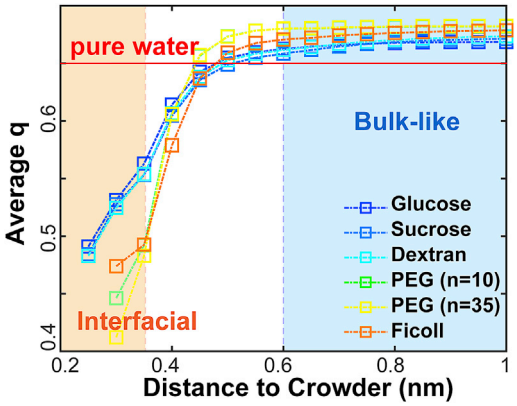

Figure 3. Correlation between tetrahedral order parameter and water-crowder distance

Average value of *q* as a function of water-crowder distance. The plot shows that H-bond structures become significantly disrupted near the crowder. But within two solvation shells away from the crowder, the structures become increasingly ordered "ice-like," showing higher tetrahedrality than even bulk water.

similarly to PEG and sucrose or glucose, respectively (Figure 3). This observation can be attributed to Ficoll supporting stronger solvent interactions compared to PEG as a result of the larger number of hydroxyls but weaker interactions compared to dextran. In contrast, dextran behaves similarly to glucose/sucrose as a result of the larger number of hydroxyl groups compared to the more highly branched Ficoll. The disorder imparted by the crowders is observed only within the first few solvation shells. Indeed, at longer distances (>0.6 nm), H-bond networks become increasingly tetrahedral for all crowded solutions, showing higher order than even pure water (Figure 3). The increase in the tetrahedral ordering via long-range interactions is most prevalent in PEG solutions. Given PEG's oxygen-oxygen distance (~2.88 Å) being similar to that of pure water at 25 °C (~2.85 Å), tetrahedral ordering is enhanced.[25,33] In other words, water structure becomes more "ice-like" in PEG solutions compared to pure water.

The observations derived from these structural analyses can be summarized as follows: (1) there are mainly two types of water structures, the more distorted interfacial water and the more ordered water at longer distances from the crowders; here referred to as "bulk water." (2) Sucrose, glucose, and dextran form stronger H-bonds with water, resulting in less disordered networks within the nearby waters. In contrast, PEG disorders local water but stabilizes global tetrahedral structures because of its geometry. (3) Surprisingly, all crowders tend to increase ordering past the first few solvation shells, suggesting that bulk water in crowded solutions adopts more ordered ice-like tetrahedral structures.

Vibrational probe

Nitrile-based vibrational probes are useful for measuring local H-bond dynamics, as the C≡N stretch is highly sensitive to the local electrostatic environment.[35] Frequency fluctuations report on the local H-bond dynamics, which can be related to the restructuring of the tetrahedral H-bond networks around the probe.[36] The present studies use thiocyanates to form H-bonds with surrounding water molecules, as depicted in Figure 4A. The C≡N stretch undergoes frequency shifts with H-bond distance and angle with respect to the molecular axis (Figure S1).[37] Ultrafast 2D IR spectroscopy is used to measure the frequency fluctuation timescales of the probes within the crowded ensembles, as described in the Experimental procedures; further, the 2D IR measurements can be compared one to one with frequency-frequency correlation functions computed from MD simulations.[11]

Although using a vibrational probe may appear to be an indirect method for accessing H-bond dynamics compared to measuring water OH stretch spectra, one

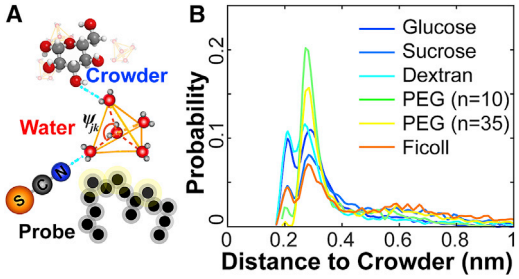

Figure 4. Interactions of thiocyanate probes with crowded solutions

(A) Cartoon depictions of thiocyanate interactions with water in crowded environments. The C≡N stretching vibration reports on its local H-bond structure and dynamics. Crowder effects on the H-bond dynamics are reflected in the C≡N frequency fluctuations, which are measured using ultrafast 2D IR spectroscopy.

(B) Distribution of SCN-crowder distances. The plots show that SCN^- dominantly samples the crowder-rich region in the aqueous solution.

complication with the latter approach is that the interfacial water response cannot easily be separated from the response of the molecules in the bulk. For instance, according to the distance-dependent order parameter analysis (Figure 3), we expect interfacial water to exhibit different dynamics compared to bulk water. Furthermore, because all crowders exhibit similar order parameter values in the bulk, we expect the dynamics of bulk water to be largely independent of the crowder. Therefore, to measure the effect of crowders on dynamics, it is essential to selectively probe the interfacial water. Fortunately, simulations indicate that thiocyanates are preferentially partitioned to the crowder interface (Figure 4B), strongly suggesting that the dynamics measured experimentally using thiocyanate as a probe primarily reports on the interfacial dynamics.

Ultrafast 2D IR spectroscopy

The subpicosecond time resolution, combined with the bond-centered structural sensitivity of ultrafast 2D IR spectroscopy, has provided an atomistic description of solvation dynamics in a wide range of molecular environments.[10,38–43] Briefly, a sequence of femtosecond laser pulses is used to measure the frequency-frequency time correlation function for the vibrational modes of interest by scanning the time delays between the excitation and detection pulses. Because the frequency fluctuations of thiocyanate are driven primarily by the dynamics of the surrounding water molecules,[44] relaxation time constants extracted from 2D IR (Figures S2–S8) represent the frequency fluctuation arising from (SCN^-HOH) H-bond dynamics and can therefore be considered a probe of the local H-bond networks (Figure 5A). The measured peak relaxation curves follow single-exponential kinetics (Figures S9 and 5B; Table S1).

Crowding effects on water dynamics

The measured relaxation time constant is the shortest in pure water (Figure 5B), indicating that the thiocyanate experiences fast H-bond rearrangements within its first solvation shell. Fast H-bond dynamics result from the relatively intact tetrahedral structure in pure water. In all crowded environments, the dynamics are slower than that of bulk water. Polymers such as PEG and Ficoll exhibit the slowest dynamics. Despite having the same chemical composition, PEG 1500 has a longer relaxation time than PEG 600 (Figure 5B). Glucose and sucrose slow the dynamics by approximately 40% compared to pure water but remain faster than the polymers. The slowdown can be attributed to strong H-bond interactions between water and sugars as a result of the hydroxyl groups, which form strong H-bonds with water. Water-crowder

Please cite this article in press as: You et al., Short- and long-range crowding effects on water's hydrogen bond networks, Cell Reports Physical Science (2021), https://doi.org/10.1016/j.xcrp.2021.100419

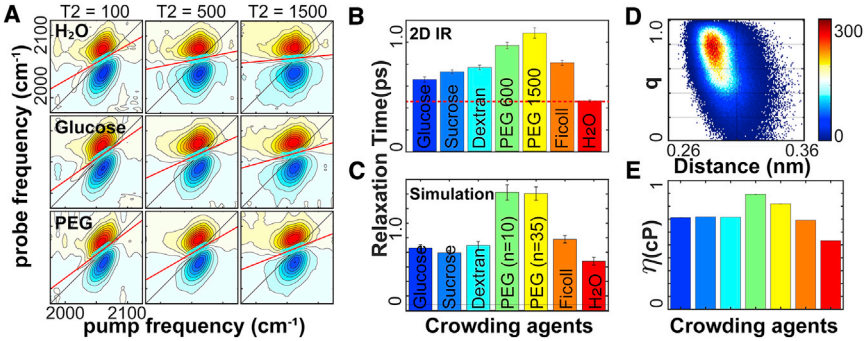

Figure 5. H-bond dynamics in crowded environments

(A) Example 2D IR spectra of C≡N stretching vibration mode in water, glucose, and PEG 1500 solutions at different waiting time delays (see Figures S2–S8 for complete dataset).

(B) Nodal-line slope decay constants obtained through the single-exponential fitting of experimental nodal-line slopes as a function of waiting time (see Figure S9).

(C) Frequency-frequency correlation functions extracted from MD simulations (see Experimental procedures and Figure S10). Error bars in (B) and (C) are the standard deviation of three independent fits to the data.

(D) Scatterplot of tetrahedral order parameter q (Equation 1) against the average distance between water oxygen to its nearest four water oxygens in the pure water simulation.

(E) Computed Stokes-Einstein viscosity of each crowder (Equation S4) for comparison with the FFCF and NLS relaxation rates.

distance analysis (Figure 3) indicates that water in glucose and sucrose solutions forms a more homogeneous network across different regimes. Although there is an increased amount of "interfacial water" in these two solutions, the H-bond network perturbation at the interface is less pronounced compared to polymers.

Computational results support 2D IR measured dynamics

Computed frequency-frequency correlation functions (FFCFs) extracted from MD simulations (Figure 5C) allow for a one-to-one comparison with the dynamics extracted from 2D IR measurements. Simulations are in excellent semiquantitative agreement with experimental 2D IR dynamics. The agreement indicates that (1) simulations accurately capture the conformational environments sampled by the probe. (2) The slowdown of water molecules imparted by the crowders is also captured by the simulations. Next, we dissect the simulation results to understand the relative effects of different crowders on the interfacial and bulk water dynamics. Heterogeneity in water dynamics can be further explored through water mean squared displacement (MSD) computed from MD trajectories (Figure S11). Viscosities, as represented by the Stokes-Einstein relation, provide an intuitive way to visualize the changes in diffusion rates (Figure 5E). PEG solutions demonstrate the slowest diffusion rates, coinciding with the experimentally measured dynamics. Numerically, the computed Stokes-Einstein viscosities for PEG solutions are approximately double that of pure water (Figure 5E), agreeing with the ~2× slowdown of the SCN^- probe in experiments. Similarly, sugars exhibit slower dynamics compared to pure water but faster compared to PEG. Thus, these analyses link the ultrafast H-bond dynamics and water diffusion rates, showing that experimental measurements are representative of water dynamics. Next, we consider the differences in water dynamics between the interfacial and bulk regions.

Water dynamics in the interfacial versus bulk regions

Combining the tetrahedral H-bond network analysis described in the previous section and the crowder effects on dynamics described here, we seek to uncover the effect of disrupted H-bond networks on local water dynamics imparted by the

crowders. Figure 5D shows the tetrahedral order parameter, q, against the average distance to the first solvation shell. The plot shows that more ordered water structures have lower oxygen-to-oxygen distances and, therefore, increased density. In the crowders, bulk water exhibits more ordered structures compared to interfacial water (Figure 3). Because disrupted H-bond networks are correlated with slower H-bond dynamics, as there are fewer donors and acceptors,[45] interfacial water should exhibit slower dynamics than the bulk. Next, we test these predictions by computing the differences between interfacial and bulk water dynamics.

Water diffusion across different regimes is explored by separating the MSD analysis for different water-crowder distance regimes (Figure S11). Although all crowders slow down diffusion compared to bulk water in the interfacial region, interfacial water dynamics across different crowders follow a similar trend as observed in the experimental and computed frequency fluctuations, which also correlate with the interfacial q values. These results reinforce the interpretation of increased structural disorder correlating with slower dynamics (Table S3). Together, the translational diffusion analyses indicate that (1) the SCN^- probe reports on dynamics at the water-crowder interface. (2) Increased hydrogen bond disorder correlates with slower dynamics, in bulk as well as at the interface. (3) Crowder-water H-bond interactions drive dynamics within local environments.

Finally, it is important to understand the effect of crowders on dynamics in the bulk region. Tables S2–S5 indicate that bulk water dynamics are similar to pure water with only subtle differences observed across crowders. Small sugar molecules have a smaller impact on the bulk water compared to polysaccharides or PEG. The above results indicate that, at long water-crowder distances, the size and the rigidity of the molecules, instead of the chemical structures, may become more dominant. Most interestingly, although the differences in bulk water dynamics in solutions compared to pure water appear subtle, they are not negligible, indicating that crowders can perturb the structure and dynamics across the entire solution.

Crowding effects on protein energy landscapes have been a focus of numerous studies; however, protein folding thermodynamics, particularly measured across different crowders, result from a combination of excluded volume, electrostatic interactions, and H-bonding, among others.[16,46] Untangling the effects of individual interactions has remained challenging.[47] The work presented here described the hydration structure and dynamics across crowders. Local dynamics are a result of disrupted H-bond networks. Analyzing the influence of molecular crowding on water H-bond structure and dynamics confirmed that crowding produces highly heterogeneous water environments.[3,11] In particular, our results are consistent with previous research indicating slow dynamics at the interface.[6,25,39,48] Interestingly, we have found that interfacial water dynamics are crowder dependent, with PEG slowing water significantly more than sugars. The fraction of interfacial water within intracellular environments can be as much as 30% of the total volume. Sugars produce a larger fraction of interfacial water due to the large surface area combined with the H-bonding interactions, producing slower overall dynamics. Polymers, however, support more bulk-like environments, as the solution is more spatially heterogeneous, exhibiting polymer-rich regions and water-rich regions.[49]

The impact of these findings can be stated within the context of biomolecular stability in crowded environments; these new findings show not only that crowders modulate the H-bond environment, but the effects produce heterogeneous H-bond ensembles, creating long-range ordered tetrahedral H-bond networks that are more ice-like than bulk water. Combined with the knowledge that protein stability

Please cite this article in press as: You et al., Short- and long-range crowding effects on water's hydrogen bond networks, Cell Reports Physical Science (2021), https://doi.org/10.1016/j.xcrp.2021.100419

is influenced by the solvent,[16,47,50] these findings present a unique opportunity to put forward an exciting new hypothesis: crowders can influence protein structure, stability, and dynamics at distances over a nanometer, through the ordering effect on the water molecules. These effects can be largely tested through more extensive molecular simulations as well as experiments to probe protein behavior within these ordered water H-bond networks.

In summary, the results show that both bulk-like and interfacial water are impacted by the crowder but through different interactions. Interfacial water exhibits slow dynamics as a result of disrupted H-bond networks. Crowders produce more ordered tetrahedral geometries compared to pure water at long distances. The insights provided by these studies are the first step to guiding the development of crowding solutions that mimic intracellular environments for *in vitro* experiments. The size and molecular makeup of the artificial crowders is important for balancing the contributions between molecular interactions and excluded volume effects. In addition, we demonstrate that the combination of ultrafast 2D IR spectroscopy and MD simulations is a powerful tool to quantitatively measure crowding effects on water structure and dynamics.

EXPERIMENTAL PROCEDURES

Resource availability

Lead contact

Further information and requests for resources should be directed to and will be fulfilled by the lead contact, Carlos Baiz (cbaiz@cm.utexas.edu).

Materials availability

This study did not generate new materials.

Data and code availability

Raw and processed experimental 2D infrared spectra, anisotropy data, and molecular dynamics simulations can be accessed via the Texas Data Repository at https://doi.org/10.18738/T8/5BA9PU.

Sample preparation

Solutions were prepared by dissolving 400 mg crowding agents in 1 mL deionized water. Crowding agents include glucose (D16-500; Fisher Scientific, NJ), sucrose (D16-500; Fisher Scientific, NJ), dextran (31388-25G; Sigma-Aldrich, MO), PEG 600 (87333-250G-F; Sigma-Aldrich, MO), PEG 1500 (A1624130; Alfa Aesar, MA), and Ficoll 70 (Bio Basics Canada, ON, Canada). NaSCN (251410; Sigma-Aldrich, MO) was then mixed with the crowding solution to the concentration of 100 mM.

FTIR spectroscopy

Absorption spectra in the C≡N stretching region were measured on a Bruker VERTEX70 Fourier transform infrared (FTIR) spectrometer. Each spectrum was the result of 32 scans at 1 cm^{-1} resolution. The sample was held between a pair of CaF_2 windows with a 50-μm PTFE spacer. Measurements were carried out at 22 °C ± 0.5 °C.

2D IR spectroscopy

Ultrafast 2D IR spectra were measured using a custom-built pulse-shaper-based spectrometer.[51] Pump and probe pulses were centered at 2,000 cm^{-1} with a FWHM of 300 cm^{-1}. Coherence times (t_1) were scanned up to 3 ps in 20 fs steps. Spectra were measured at a series of waiting times, t_2, from 50 fs to 5,000 fs. The probe pulse was dispersed into a 128 × 128-pixel MCT array to generate the detection axis (Figure S12). Nodal line slope (NLS) analysis[52] was performed on all the

spectra. The NLS was calculated by mapping the probe frequency, ω_3, at each pump frequency, ω_1, corresponding to the node between the positive and negative peak. The resulting scatterplots are fit to a line, and the slope is extracted from each fit. Spectra were collected in the parallel and perpendicular polarization conditions. The isotropic (iso) 2D IR spectra are computed from the parallel (para) and perpendicular (perp) polarization spectra as $S_{iso}(t_2) = (1/3) * (S_{para}(t_2) + 2S_{perp}(t_2))$.

Molecular dynamics simulations

Molecular dynamics simulations were carried out using the GROMACS package[53] employing the CHARMM 36 general force-field.[54] Simulation boxes were created using PACKMOL[55] and contained 4,000 TIP4P-Ew water molecules, 8 Na^+, 8 SCN^-, and approximately 30% by weight of crowder molecules to correspond with the experimental conditions. The chemical formula of each crowder molecule is shown in Figure 1B. Each box was run through an initial, 5,000-step, steepest-descent energy minimization with a Verlet cutoff scheme. The minimization was followed by 100 ps of NVT equilibration and velocity rescaling temperature coupling at 303.15 K. Next, NPT equilibration was performed for 10 ns at 303.15 K, Nose-Hoover temperature coupling, and Parrinello-Rahman pressure coupling. All bonds were constrained with the LINCS algorithm. The large polymers, such as PEG (n = 35) and dextran, went through double minimization and NVT equilibration, as well as an additional NPT equilibration. Production simulations (5 ns) were carried out using the same parameters as the NPT equilibration. Trajectories were saved every 10 ps for order parameter and distance analyses (Figures 2, 3, 4B, and 5D). Each box was further run through ten 100-ps simulations sampled at 10-fs increments to extract dynamical information (Figures 5C and 5E).

Hydrogen bond network analysis

The percentage of bulk water, average participation ratio, network entropy, and tetrahedral order parameters were defined by network analysis using an adjacency matrix and relative geometries as described in the supporting information. Water-crowder distance analyses included the nearest radial distance between the water oxygen and any non-hydrogen crowder atom.

Frequency fluctuations

FFCFs were determined with the equation $C(t) = \langle \omega(0)\omega(t) \rangle$. To calculate the frequency trajectories, the thiocyanate vibrational map developed by Cho was used.[37] Within each crowder system, ten 100-ps simulations with a 10-fs sampling rate were run sequentially after the production run using the same MD simulation conditions. In accordance with the frequency map, the potential was calculated on every thiocyanate ion for every frame. Thiocyanate and sodium ions were excluded from the electrostatic calculations. Furthermore, the charges on the water molecule were altered to the ChelpG charges used by Cho and coworkers for parameterizing the map.[35] The autocorrelations (Figure S10) were fit to a biexponential decay with an offset. Only the picosecond component is compared to experiment because shorter or longer timescale components cannot be measured using our experimental setup.

SUPPLEMENTAL INFORMATION

Supplemental information can be found online at https://doi.org/10.1016/j.xcrp.2021.100419.

ACKNOWLEDGMENTS

This work has been supported by the Welch Foundation (F-1891) and the National Science Foundation (CHE-1847199).

Please cite this article in press as: You et al., Short- and long-range crowding effects on water's hydrogen bond networks, Cell Reports Physical Science (2021), https://doi.org/10.1016/j.xcrp.2021.100419

AUTHOR CONTRIBUTIONS

Conceptualization, C.R.B. and X.Y.; methodology, X.Y. and J.C.S.; software, X.Y. and J.C.S.; investigation, X.Y.; formal analysis, X.Y.; resources, X.Y. and C.R.B.; writing – original draft, X.Y.; writing – review & editing, all authors; funding acquisition, C.R.B.; supervision, C.R.B.

DECLARATION OF INTERESTS

The authors declare no competing interests.

Received: February 25, 2021
Revised: March 24, 2021
Accepted: April 7, 2021
Published: April 27, 2021

REFERENCES

1. Harada, R., Sugita, Y., and Feig, M. (2012). Protein crowding affects hydration structure and dynamics. J. Am. Chem. Soc. *134*, 4842–4849.

2. Ellis, R.J., and Minton, A.P. (2003). Cell biology: join the crowd. Nature *425*, 27–28.

3. Feig, M., Yu, I., Wang, P.H., Nawrocki, G., and Sugita, Y. (2017). Crowding in cellular environments at an atomistic level from computer simulations. J. Phys. Chem. B *121*, 8009–8025.

4. Weiss, M. (2014). Chapter Eleven - Crowding, diffusion, and biochemical reactions. In International Review of Cell and Molecular Biology, R. Hancock and K.W. Jeon, eds. (Academic), pp. 383–417.

5. Mukherjee, S., Waegele, M.M., Chowdhury, P., Guo, L., and Gai, F. (2009). Effect of macromolecular crowding on protein folding dynamics at the secondary structure level. J. Mol. Biol. *393*, 227–236.

6. Tros, M., Zheng, L., Hunger, J., Bonn, M., Bonn, D., Smits, G.J., and Woutersen, S. (2017). Picosecond orientational dynamics of water in living cells. Nat. Commun. *8*, 904.

7. Bellissent-Funel, M.C., Hassanali, A., Havenith, M., Henchman, R., Pohl, P., Sterpone, F., van der Spoel, D., Xu, Y., and Garcia, A.E. (2016). Water determines the structure and dynamics of proteins. Chem. Rev. *116*, 7673–7697.

8. Templeton, C., and Elber, R. (2018). Why does RNA collapse? The importance of water in a simulation study of helix-junction-helix systems. J. Am. Chem. Soc. *140*, 16948–16951.

9. Conti Nibali, V., and Havenith, M. (2014). New insights into the role of water in biological function: studying solvated biomolecules using terahertz absorption spectroscopy in conjunction with molecular dynamics simulations. J. Am. Chem. Soc. *136*, 12800–12807.

10. Flanagan, J.C., Cardenas, A.E., and Baiz, C.R. (2020). Ultrafast spectroscopy of lipid-water interfaces: transmembrane crowding drives H-bond dynamics. J. Phys. Chem. Lett. *11*, 4093–4098.

11. Verma, P.K., Kundu, A., Ha, J.H., and Cho, M. (2016). Water dynamics in cytoplasm-like crowded environment correlates with the conformational transition of the macromolecular crowder. J. Am. Chem. Soc. *138*, 16081–16088.

12. Ebel, C., Eisenberg, H., and Ghirlando, R. (2000). Probing protein-sugar interactions. Biophys. J. *78*, 385–393.

13. Mukherjee, S.K., Gautam, S., Biswas, S., Kundu, J., and Chowdhury, P.K. (2015). Do macromolecular crowding agents exert only an excluded volume effect? A protein solvation study. J. Phys. Chem. B *119*, 14145–14156.

14. Cordone, L., Cottone, G., and Giuffrida, S. (2007). Role of residual water hydrogen bonding in sugar/water/biomolecule systems: a possible explanation for *trehalose peculiarity*. J. Phys. Condens. Matter *19*, 205110.

15. Verkman, A.S. (2002). Solute and macromolecule diffusion in cellular aqueous compartments. Trends Biochem. Sci. *27*, 27–33.

16. Wang, Y., Sarkar, M., Smith, A.E., Krois, A.S., and Pielak, G.J. (2012). Macromolecular crowding and protein stability. J. Am. Chem. Soc. *134*, 16614–16618.

17. Lu, C., Prada-Gracia, D., and Rao, F. (2014). Structure and dynamics of water in crowded environments slows down peptide conformational changes. J. Chem. Phys. *141*, 045101.

18. Breydo, L., Sales, A.E., Frege, T., Howell, M.C., Zaslavsky, B.Y., and Uversky, V.N. (2015). Effects of polymer hydrophobicity on protein structure and aggregation kinetics in crowded milieu. Biochemistry *54*, 2957–2966.

19. Kuznetsova, I.M., Zaslavsky, B.Y., Breydo, L., Turoverov, K.K., and Uversky, V.N. (2015). Beyond the excluded volume effects: mechanistic complexity of the crowded milieu. Molecules *20*, 1377–1409.

20. Gnutt, D., and Ebbinghaus, S. (2016). The macromolecular crowding effect–from in vitro into the cell. Biol. Chem. *397*, 37–44.

21. Senske, M., Törk, L., Born, B., Havenith, M., Herrmann, C., and Ebbinghaus, S. (2014). Protein stabilization by macromolecular crowding through enthalpy rather than entropy. J. Am. Chem. Soc. *136*, 9036–9041.

22. Sarkar, M., Li, C., and Pielak, G.J. (2013). Soft interactions and crowding. Biophys. Rev. *5*, 187–194.

23. Hingorani, K.S., and Gierasch, L.M. (2014). Comparing protein folding in vitro and in vivo: foldability meets the fitness challenge. Curr. Opin. Struct. Biol. *24*, 81–90.

24. Ensing, B., Tiwari, A., Tros, M., Hunger, J., Domingos, S.R., Pérez, C., Smits, G., Bonn, M., Bonn, D., and Woutersen, S. (2019). On the origin of the extremely different solubilities of polyethers in water. Nat. Commun. *10*, 2893.

25. Daley, K.R., and Kubarych, K.J. (2017). An "iceberg" coating preserves bulk hydration dynamics in aqueous PEG solutions. J. Phys. Chem. B *121*, 10574–10582.

26. Rubinson, K.A., and Meuse, C.W. (2013). Deep hydration: poly(ethylene glycol) M_W 2000–8000 Da probed by vibrational spectrometry and small-angle neutron scattering and assignment of ΔG° to individual water layers. Polymer *54*, 709–723.

27. Gonzalez-Tello, P., Camacho, F., and Blazquez, G. (1994). Density and viscosity of concentrated aqueous solutions of polyethylene glycol. J. Chem. Eng. Data *39*, 611–614.

28. Truskett, T.M., Torquato, S., and Debenedetti, P.G. (2000). Towards a quantification of disorder in materials: distinguishing equilibrium and glassy sphere packings. Phys. Rev. E Stat. Phys. Plasmas Fluids Relat. Interdiscip. Topics *62* (1 Pt B), 993–1001.

29. Errington, J.R., and Debenedetti, P.G. (2001). Relationship between structural order and the anomalies of liquid water. Nature *409*, 318–321.

30. Chau, P.-L., and Hardwick, A.J. (1998). A new order parameter for tetrahedral configurations. Mol. Phys. *93*, 511–518.

31. Duboué-Dijon, E., and Laage, D. (2015). Characterization of the local structure in liquid water by various order parameters. J. Phys. Chem. B *119*, 8406–8418.

32. Sigala, P.A., Ruben, E.A., Liu, C.W., Piccoli, P.M., Hohenstein, E.G., Martínez, T.J., Schultz,

A.J., and Herschlag, D. (2015). Determination of hydrogen bond structure in water versus aprotic environments to test the relationship between length and stability. J. Am. Chem. Soc. *137*, 5730–5740.

33. Kjellander, R., and Florin, E. (1981). Water structure and changes in thermal stability of the system poly(ethylene oxide)–water. J. Chem. Soc., Far. Trans.: Phys. Chem. Condens. Phases *77*, 2053–2077.

34. Israelachvili, J. (1997). The different faces of poly(ethylene glycol). Proc. Natl. Acad. Sci. USA *94*, 8378–8379.

35. Baiz, C.R., Błasiak, B., Bredenbeck, J., Cho, M., Choi, J.H., Corcelli, S.A., Dijkstra, A.G., Feng, C.J., Garrett-Roe, S., Ge, N.H., et al. (2020). Vibrational spectroscopic map, vibrational spectroscopy, and intermolecular interaction. Chem. Rev. *120*, 7152–7218.

36. Okuda, M., Higashi, M., Ohta, K., Saito, S., and Tominaga, K. (2018). Theoretical investigation on vibrational frequency fluctuations of SCN-derivatized vibrational probe molecule in water. Chem. Phys. *512*, 82–87.

37. Lee, H., Choi, J.H., and Cho, M. (2010). Vibrational solvatochromism and electrochromism of cyanide, thiocyanate, and azide anions in water. Phys. Chem. Chem. Phys. *12*, 12658–12669.

38. Oh, K.I., You, X., Flanagan, J.C., and Baiz, C.R. (2020). Liquid-liquid phase separation produces fast H-bond dynamics in DMSO-water mixtures. J. Phys. Chem. Lett. *11*, 1903–1908.

39. Roget, S.A., Kramer, P.L., Thomaz, J.E., and Fayer, M.D. (2019). Bulk-like and interfacial water dynamics in nafion fuel cell membranes investigated with ultrafast nonlinear IR spectroscopy. J. Phys. Chem. B *123*, 9408–9417.

40. Cunha, A.V., Salamatova, E., Bloem, R., Roeters, S.J., Woutersen, S., Pshenichnikov, M.S., and Jansen, T.L.C. (2017). Interplay between hydrogen bonding and vibrational coupling in liquid N-methylacetamide. J. Phys. Chem. Lett. *8*, 2438–2444.

41. Salamatova, E., Cunha, A.V., Bloem, R., Roeters, S.J., Woutersen, S., Jansen, T.L.C., and Pshenichnikov, M.S. (2018). Hydrophobic collapse in N-methylacetamide-water mixtures. J. Phys. Chem. A *122*, 2468–2478.

42. Kundu, A., Verma, P.K., and Cho, M. (2019). Water structure and dynamics in the stern layer of micelles: femtosecond mid-infrared pump-probe spectroscopy study. J. Phys. Chem. B *123*, 5238–5245.

43. Perakis, F., Marco, L.D., Shalit, A., Tang, F., Kann, Z.R., Kühne, T.D., Torre, R., Bonn, M., and Nagata, Y. (2016). Vibrational spectroscopy and dynamics of water. Chem. Rev. *116*, 7590–7607.

44. Nishida, J., Breen, J.P., Lindquist, K.P., Umeyama, D., Karunadasa, H.I., and Fayer, M.D. (2018). Dynamically disordered lattice in a layered Pb-I-SCN perovskite thin film probed by two-dimensional infrared spectroscopy. J. Am. Chem. Soc. *140*, 9882–9890.

45. Moilanen, D.E., Fenn, E.E., Lin, Y.S., Skinner, J.L., Bagchi, B., and Fayer, M.D. (2008). Water inertial reorientation: hydrogen bond strength and the angular potential. Proc. Natl. Acad. Sci. USA *105*, 5295–5300.

46. Feig, M., and Sugita, Y. (2012). Variable interactions between protein crowders and biomolecular solutes are important in understanding cellular crowding. J. Phys. Chem. B *116*, 599–605.

47. Breydo, L., Reddy, K.D., Piai, A., Felli, I.C., Pierattelli, R., and Uversky, V.N. (2014). The crowd you're in with: effects of different types of crowding agents on protein aggregation. Biochim. Biophys. Acta *1844*, 346–357.

48. Fogarty, A.C., and Laage, D. (2014). Water dynamics in protein hydration shells: the molecular origins of the dynamical perturbation. J. Phys. Chem. B *118*, 7715–7729.

49. Lee, H., Venable, R.M., Mackerell, A.D., Jr., and Pastor, R.W. (2008). Molecular dynamics studies of polyethylene oxide and polyethylene glycol: hydrodynamic radius and shape anisotropy. Biophys. J. *95*, 1590–1599.

50. Miklos, A.C., Sarkar, M., Wang, Y., and Pielak, G.J. (2011). Protein crowding tunes protein stability. J. Am. Chem. Soc. *133*, 7116–7120.

51. Edington, S.C., Gonzalez, A., Middendorf, T.R., Halling, D.B., Aldrich, R.W., and Baiz, C.R. (2018). Coordination to lanthanide ions distorts binding site conformation in calmodulin. Proc. Natl. Acad. Sci. USA *115*, E3126–E3134.

52. Guo, Q., Pagano, P., Li, Y.L., Kohen, A., and Cheatum, C.M. (2015). Line shape analysis of two-dimensional infrared spectra. J. Chem. Phys. *142*, 212427.

53. Berendsen, H.J.C., van der Spoel, D., and van Drunen, R. (1995). GROMACS: a message-passing parallel molecular dynamics implementation. Comput. Phys. Commun. *91*, 43–56.

54. Oh, K.-I., and Baiz, C.R. (2019). Empirical S=O stretch vibrational frequency map. J. Chem. Phys. *151*, 234107.

55. Martínez, L., Andrade, R., Birgin, E.G., and Martínez, J.M. (2009). PACKMOL: a package for building initial configurations for molecular dynamics simulations. J. Comput. Chem. *30*, 2157–2164.

Cell Reports Physical Science, Volume *2*

Supplemental information

Short- and long-range crowding effects on water's hydrogen bond networks

Xiao You, Joseph C. Shirley, Euihyun Lee, and Carlos R. Baiz

SUPPORTING INFORMATION

S1. INFRARED ABSORPTION SPECTROSCOPY

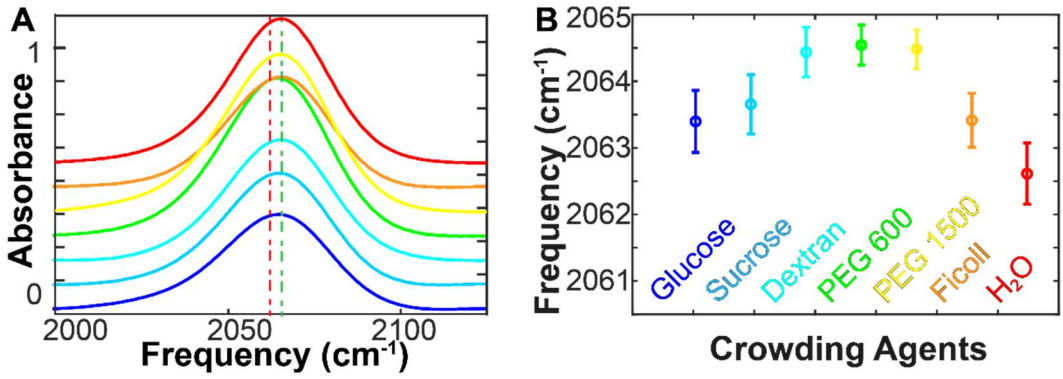

Figure S1. **A.** Normalized FTIR spectra of thiocyanate anion in 30% crowded solutions; **B.** Peak positions and error bars representing 99% confidence intervals obtained through Lorentzian fits to the spectra. Spectra and frequencies are represented in the same colors in both panels.

Center frequencies and widths of the IR absorption band report the distribution of microenvironments. The shift of C≡N stretching vibration indicates that the local aqueous environment is only minorly altered by the crowding agents. As shown in **Figure S1B**, when compared to H_2O, the C≡N stretch shifted to higher frequencies. Since the vibrational frequency is influenced by many parameters such as polarity, H-bonding strength, the distance and angle of the H-bond and number of H-bonds, many of which can produce band shifts in opposite directions, the relationship between frequencies and local solvation environments is not straightforward.[1-3]

S2. EXPERIMENTAL 2D IR SPECTRA

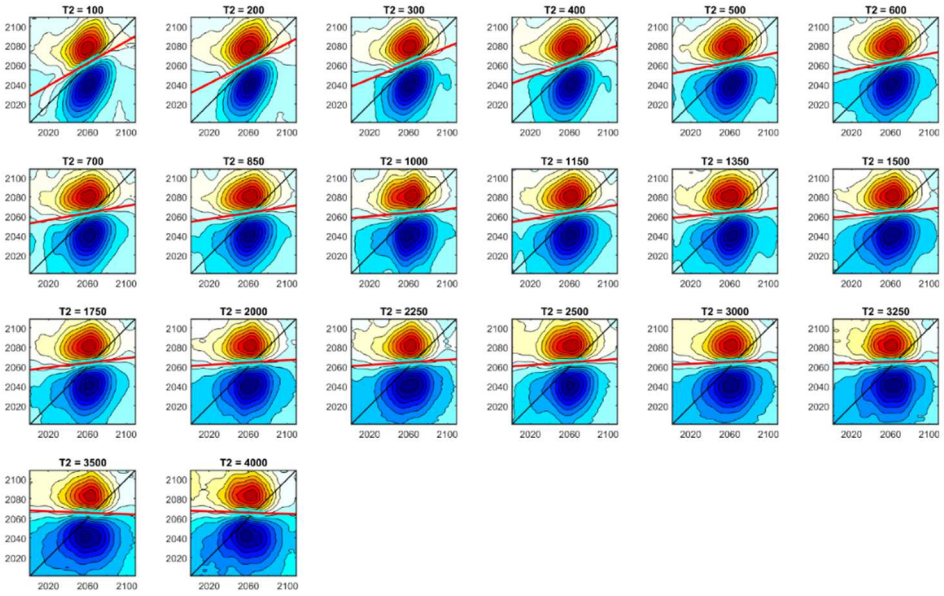

Figure S2. Experimental 2D IR contour maps and nodal-line-slope (NLS) fitting of C≡N stretching vibration mode of thiocyanate in H_2O solution at different waiting time delays (t_2) in fs as indicated above each plot. The horizontal axis represents the excitation frequency (cm^{-1}) and the vertical axis represents the detection frequency (cm^{-1}) as illustrated in Figure S12. The fitted nodal-line is shown in red.

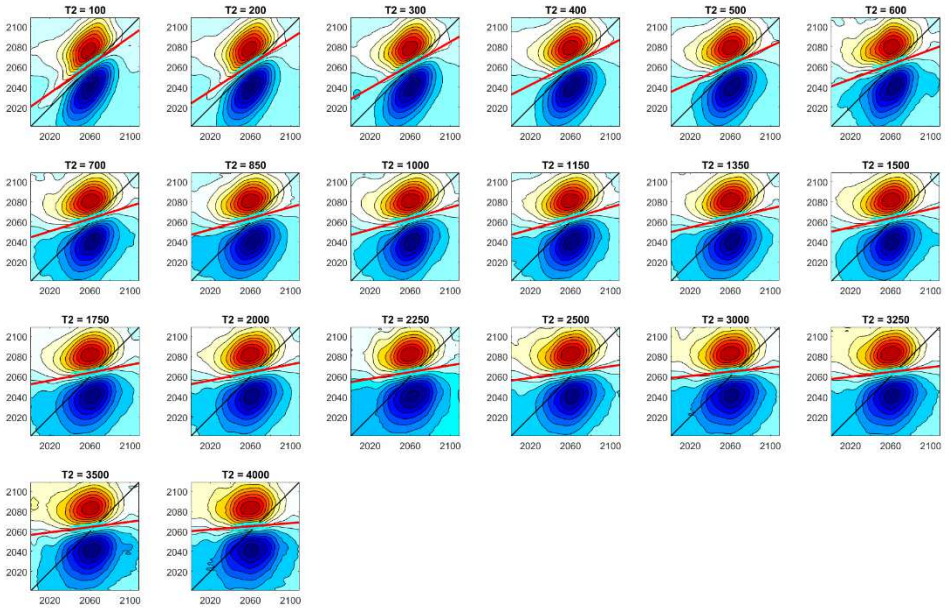

Figure S3. Experimental 2D IR contour maps and NLS fitting of C≡N stretching vibration mode of thiocyanate in glucose H_2O solution at different waiting time delays (t_2) in fs as indicated above each plot. The horizontal axis represents the excitation frequency (cm^{-1}) and the vertical axis represents the detection frequency (cm^{-1}) as illustrated in Figure S12. The fitted nodal-line is shown in red.

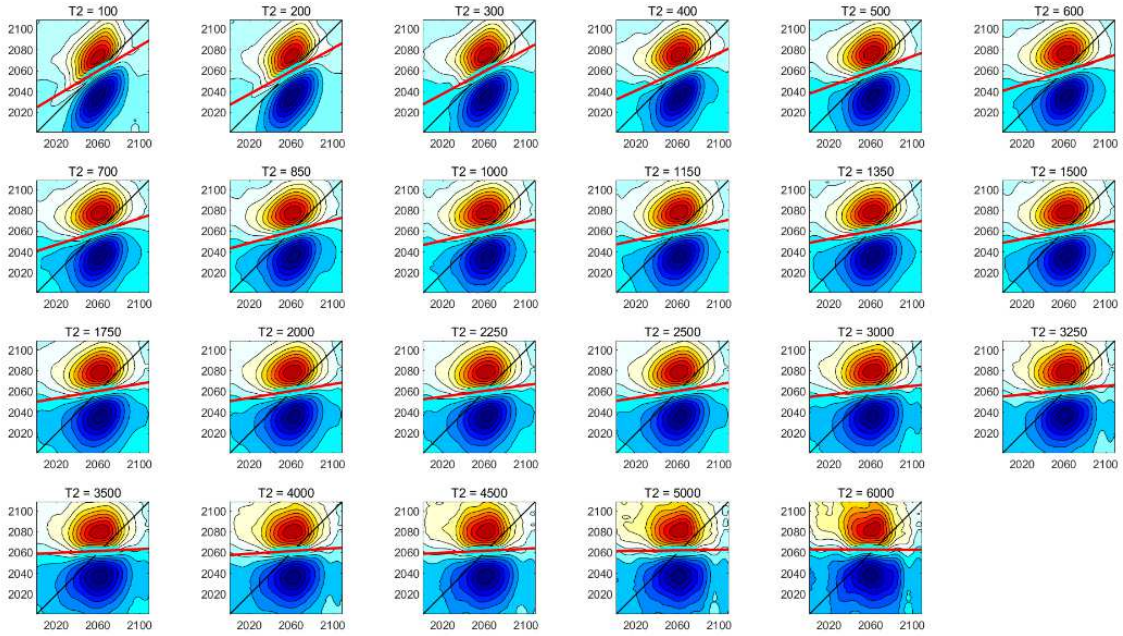

Figure S4. Experimental 2D IR contour maps and NLS fitting of C≡N stretching vibration mode of thiocyanate in sucrose H_2O solution at different waiting time delays (t_2) in fs as indicated above each plot. The horizontal axis represents the excitation frequency (cm^{-1}) and the vertical axis represents the detection frequency (cm^{-1}) as illustrated in Figure S12. The fitted nodal-line is shown in red.

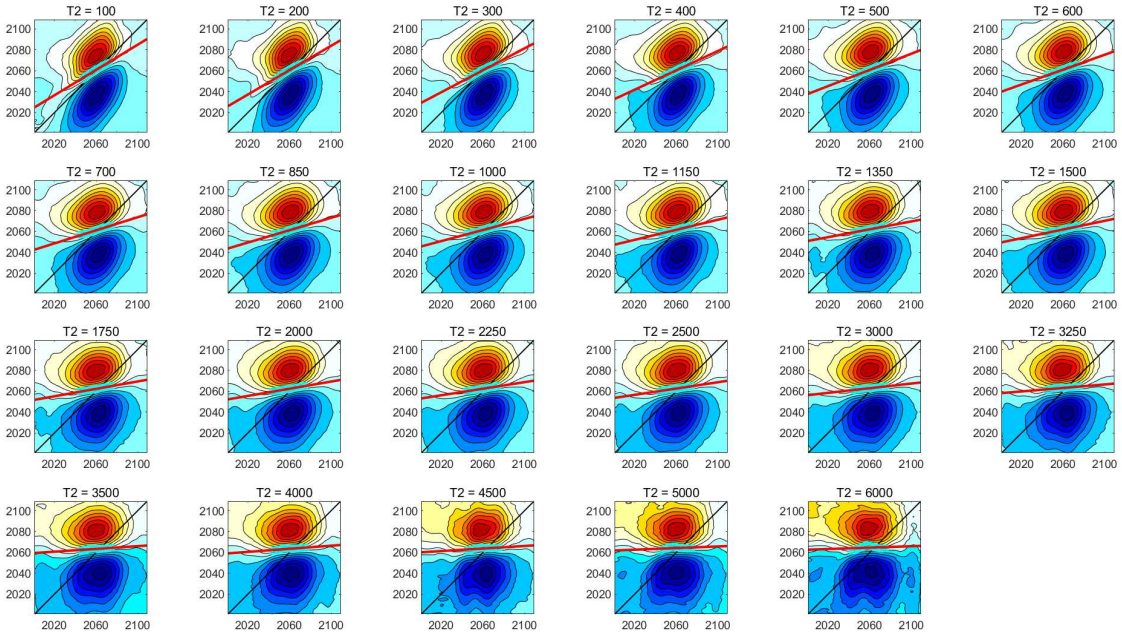

Figure S5. Experimental 2D IR contour maps and NLS fitting of C≡N stretching vibration mode of thiocyanate in dextran H_2O solution at different waiting time delays (t_2) in fs as indicated above each plot. The horizontal axis represents the excitation frequency (cm^{-1}) and the vertical axis represents the detection frequency (cm^{-1}) as illustrated in Figure S12. The fitted nodal-line is shown in red.

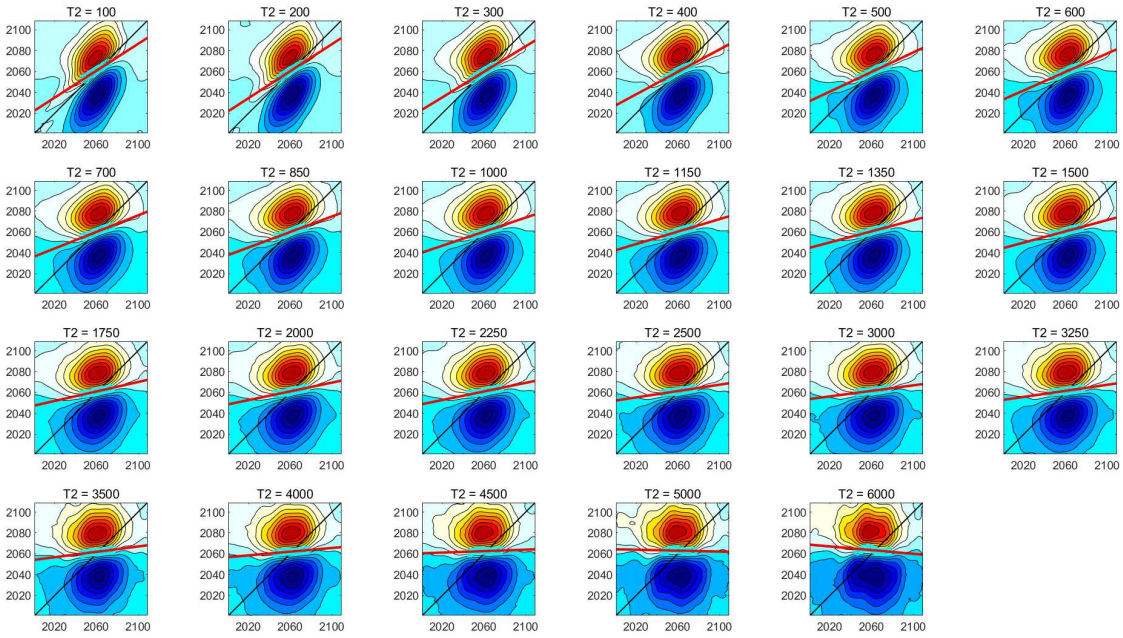

Figure S6. Experimental 2D IR contour maps and NLS fitting of C≡N stretching vibration mode of thiocyanate in PEG 600 H_2O solution at different waiting time delays (t_2) in fs as indicated above each plot. The horizontal axis represents the excitation frequency (cm^{-1}) and the vertical axis represents the detection frequency (cm^{-1}) as illustrated in Figure S12. The fitted nodal-line is shown in red.

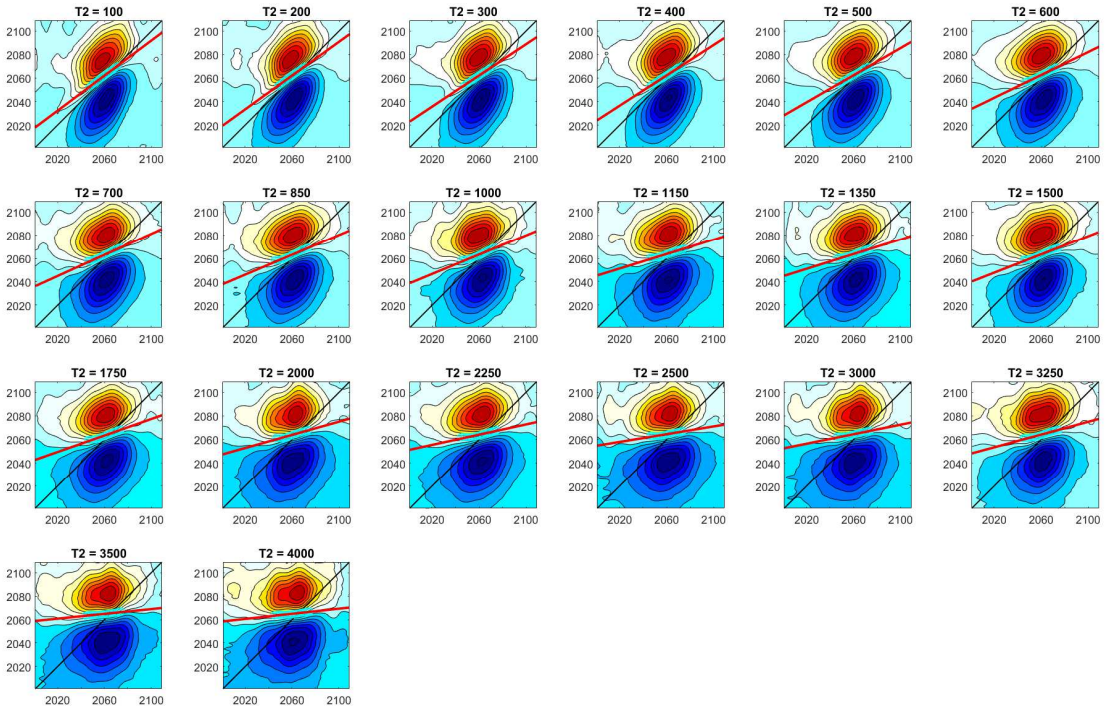

Figure S7. Experimental 2D IR contour maps and NLS fitting of C≡N stretching vibration mode of thiocyanate in PEG 1500 H_2O solution at different waiting time delays (t_2) in fs as indicated above each plot. The horizontal axis represents the excitation frequency (cm^{-1}) and the vertical axis represents the detection frequency (cm^{-1}) as illustrated in Figure S12. The fitted nodal-line is shown in red.

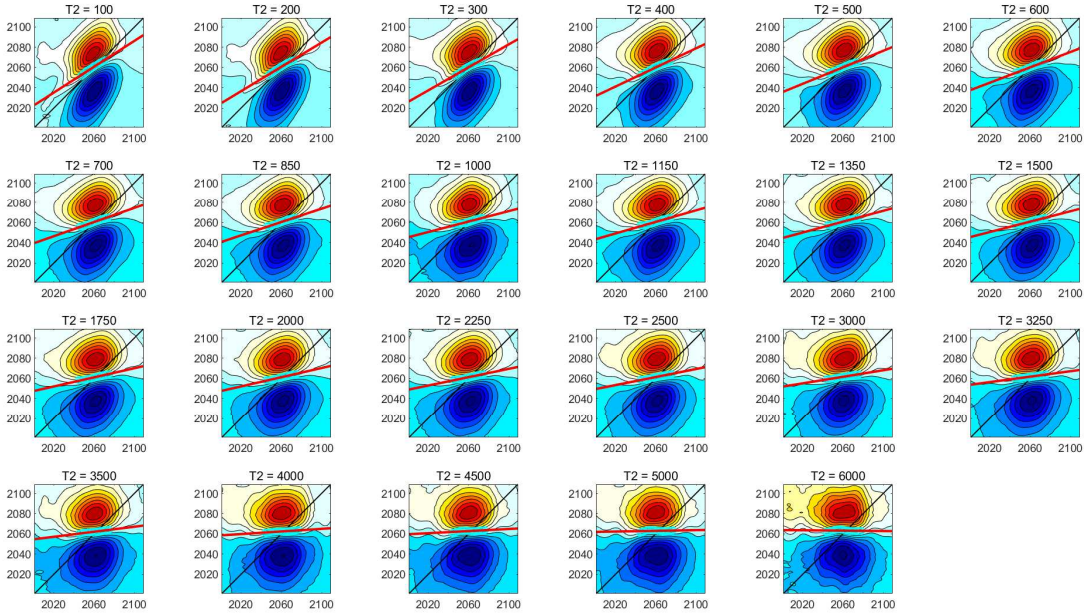

Figure S8. Experimental 2D IR contour maps and NLS fitting of C≡N stretching vibration mode of thiocyanate in Ficoll 70 H_2O solution at different waiting time delays (t_2) in fs as indicated above each plot. The horizontal axis represents the excitation frequency (cm^{-1}) and the vertical axis represents the detection frequency (cm^{-1}) as illustrated in Figure S12. The fitted nodal-line is shown in red.

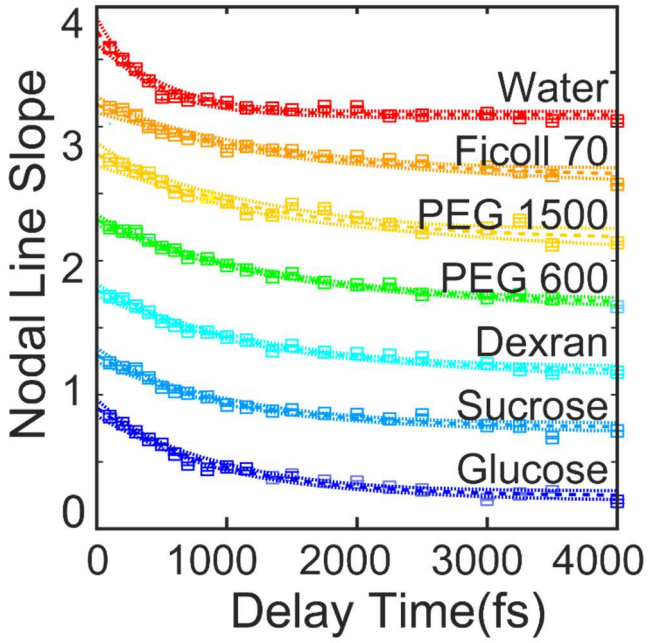

Figure S9. NLS decay curves of each sample extracted from 2D IR Spectra (Figures S2-8). Decay constants in **Figure 5** are obtained through single-exponential fitting on NLS curves as indicated by the dashed line. The curves are vertically offset for clarity.

Table S1

Crowders	Amplitudes	Timescales of H-bond dynamics	Amplitude of long-time dynamics
	a_1	b_2 (fs)	c
Glucose	0.83	0.65	0.12
Sucrose	0.77	0.72	0.10
Dextran	0.79	0.76	0.10
PEG 600	0.80	0.96	0.11
PEG 1500	0.83	1.08	0.14
Ficoll70	0.75	0.80	0.14
Water	0.78	0.46	0.02

Table S1. Fitting results of NLS decay curves with bi-exponential fitting function:

$$f(t) = a \times e^{-t/b} + c. \qquad \text{SI Eq. 1}$$

Where a represent the coefficient of the exponential terms; b is the decay constant in **Figure 5**. The static inhomogeneity is encapsulated as the coefficient c in the equation.

S3. ANALYSIS OF MOLECULAR DYNAMICS TRAJECTORIES

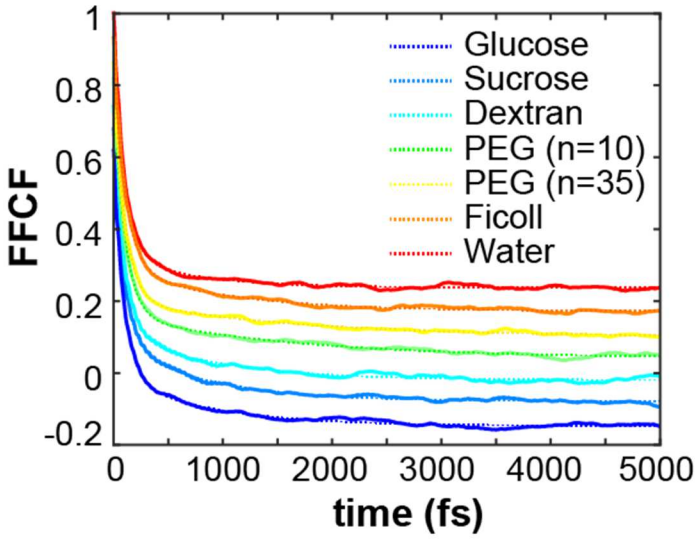

Figure S10. Normalized frequency-frequency correlation function (FFCF) and fitted curve (dotted line) of each sample at various delay time. Decay constants in Figure 5C are obtained through bi-exponential fitting on NLS curves. See **Table S1** for fitting parameters. The curves are vertically offset for clarity.

Table S2

Crowders	Amplitudes		Timescales of H-bond dynamics		Amplitude of long-time dynamics
	a_1	a_2	b_1 (fs)	b_2 (fs)	c
Glucose	0.805	0.180	92	856	0.006
Sucrose	0.749	0.222	90	792	0.019
Dextran	0.793	0.179	92	893	0.014
PEG (n = 10)	0.839	0.156	99	1623	0.008
PEG (n = 35)	0.845	0.132	98	1607	0.012
Ficoll70	0.808	0.164	101	978	0.015
Water	0.860	0.124	94	678	0.010

Table S1. Fitting results of FFCF curves with bi-exponential fitting function:

$$f(t) = a_1 e^{-t/b_1} + a_2 e^{-t/b_2} + c. \qquad \text{SI Eq. 1}$$

Where a_1 and a_2 represent the coefficient of the exponential terms; b_1 and b_2 represent a fast (<200 fs) decay (b_1) and a picosecond H-bond decay (b_2). The picosecond dynamics are compared with experiment as described in the main text. The static inhomogeneity is encapsulated as the coefficient c in the equation.

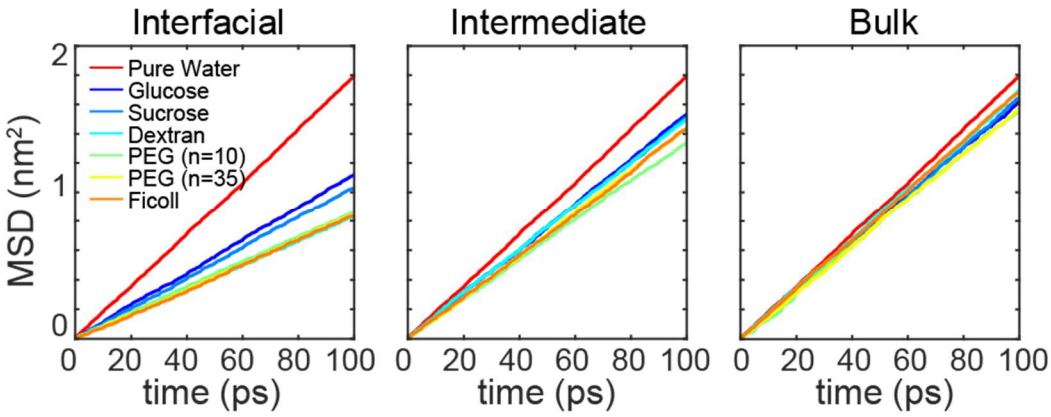

Figure S11. Mean square displacement (MSD) calculated from molecular dynamic (MD) simulation for each crowding solution with a 5 ps restart time and 10 fs interval time. MSD of pure water is included in each graph for reference. The diffusion rate increases as waters move from interfacial to bulk. At the interface, sucrose- and glucose-crowded water exhibit the fastest dynamics. In the intermediate and bulk regions, the differences between diffusion rates became subtle.

Table S2 All water

Total	a (nm^2/s)	b (nm)	a std	b std	η (cP)	η err
water	2.81E-06	6.40E-03	6.32E-08	3.19E-04	0.563	0.013
glucose	2.03E-06	7.15E-03	8.98E-08	3.60E-04	0.779	0.035

sucrose	2.02E-06	7.18E-03	6.03E-08	3.91E-04	0.781	0.023
dextran	2.03E-06	7.24E-03	8.63E-08	5.19E-04	0.778	0.033
PEG (n=10)	1.54E-06	8.01E-03	2.81E-08	3.65E-04	1.029	0.019
PEG (n=35)	1.70E-06	7.88E-03	5.62E-08	3.59E-04	0.932	0.031
Ficoll	2.09E-06	7.12E-03	6.38E-08	4.66E-04	0.755	0.023

Table S3 Interfacial water

Interfacial	a (nm^2/s)	b (nm)	a std	b std	η (cP)	η err
water	2.81E-06	6.40E-03	6.32E-08	3.19E-04	0.563	0.013
glucose	1.65E-06	7.56E-03	6.00E-08	4.98E-04	0.955	0.035
sucrose	1.48E-06	7.87E-03	6.18E-08	2.88E-04	1.065	0.044
dextran	1.20E-06	7.16E-03	9.22E-08	7.25E-04	1.318	0.101
PEG (n=10)	1.18E-06	8.44E-03	1.62E-08	1.90E-04	1.344	0.019
PEG (n=35)	1.14E-06	8.54E-03	6.88E-08	4.60E-04	1.382	0.083
Ficoll	1.16E-06	7.88E-03	7.77E-08	9.21E-04	1.365	0.092

Table S4 Intermediate Water

Intermediate	a (nm^2/s)	b (nm)	a std	b std	η (cP)	η err
water	2.81E-06	6.40E-03	6.32E-08	3.19E-04	0.563	0.013
glucose	2.37E-06	6.65E-03	1.11E-07	8.79E-04	0.666	0.031
sucrose	2.35E-06	6.59E-03	7.43E-08	5.95E-04	0.672	0.021
dextran	2.28E-06	6.94E-03	1.31E-07	1.13E-03	0.692	0.040
PEG (n=10)	2.05E-06	7.22E-03	8.33E-08	4.69E-04	0.771	0.031
PEG (n=35)	2.20E-06	7.09E-03	6.38E-08	5.52E-04	0.718	0.021
Ficoll	2.22E-06	7.20E-03	1.53E-07	9.60E-04	0.711	0.049

Table S5 Bulk water

Bulk	a (nm^2/s)	b (nm)	a std	b std	η (cP)	η err
water	2.81E-06	6.40E-03	6.32E-08	3.19E-04	0.563	0.013
glucose	2.46E-06	7.07E-03	1.87E-07	3.04E-04	0.643	0.049
sucrose	2.54E-06	6.85E-03	1.90E-07	9.42E-04	0.622	0.046
dextran	2.60E-06	7.53E-03	9.85E-08	6.57E-04	0.607	0.023
PEG (n=10)	2.28E-06	7.92E-03	1.53E-07	3.36E-03	0.694	0.047
PEG (n=35)	2.44E-06	7.33E-03	1.28E-07	7.07E-04	0.647	0.034
Ficoll	2.64E-06	6.56E-03	1.11E-07	7.59E-04	0.598	0.025

Tables S2-5. Fitting results of MSD plots in **Figure S11**, with linear fitting function: $y = ax + b$, where a represents displacement D in the unit of nm^2/s. Viscosity calculated using the Stokes-Einstein Relation

where k_B represents the Boltzmann constant, T the temperature, and r is the radius of a water molecule, assumed to be 1.4 Angstroms. Note that the viscosity constants are only calculated for visualization purposes. The diffusion constants, computed across crowders, contain the same information as the viscosity.

$$\eta = \frac{k_B T}{6\pi D r} = \frac{\left(1.38064852*10^{-23}\,\frac{\mathrm{kg}\cdot\mathrm{m}^2}{\mathrm{s}^2\cdot\mathrm{K}}\right)\cdot(303.15\ \mathrm{K})}{6\pi\cdot\left(2.979*10^{-9}\frac{\mathrm{m}^2}{\mathrm{s}}\right)\cdot(1.4*10^{-10}\ \mathrm{m})} = 5.32*10^{-4}\,\frac{\mathrm{kg}}{\mathrm{m}\cdot\mathrm{s}} = 0.532\ \mathrm{cP} \qquad \text{SI Eq. 2}$$

$$\eta = \frac{1.58603*10^{-9}}{\left(D\ \mathrm{in}\frac{\mathrm{m}^2}{\mathrm{s}}\right)}\ \mathrm{cP} = \frac{1.58603*10^{-6}}{D\ (\frac{\mathrm{nm}^2}{\mathrm{fs}})}\ \mathrm{cP} \qquad \text{SI Eq. 3}$$

$$\Delta\eta = \left|\frac{d\eta}{dD}\right|\Delta D = \frac{1.58603*10^{-6}}{\left(D\ \mathrm{in}\frac{\mathrm{nm}^2}{\mathrm{fs}}\right)^2} * \left(\Delta D\ \mathrm{in}\,\frac{\mathrm{nm}^2}{\mathrm{fs}}\right) \qquad \text{SI Eq. 4}$$

S4. ILLUSTRATION OF EXPERIMENTAL SETUP

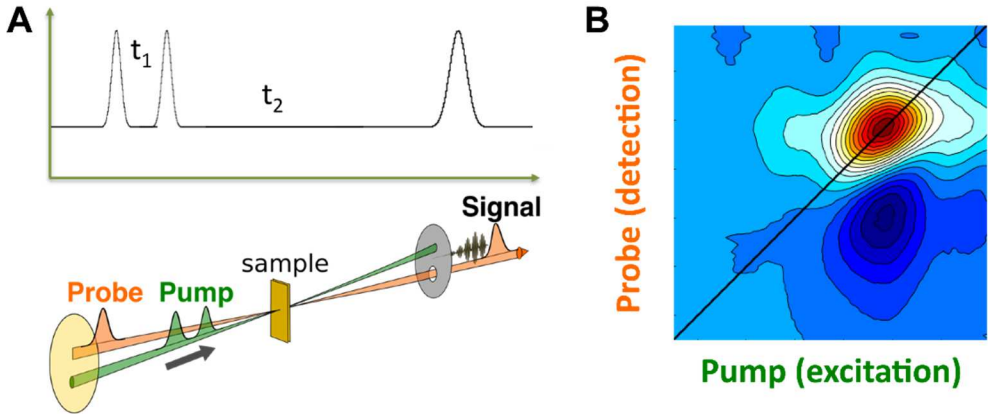

Figure S12. A. Illustration of 2D IR experimental setup in the pump-probe geometry. **B.** Representative 2D IR spectrum. In our 2D IR setup, three laser pulses create a nonlinear polarization in the sample. Two pump pulses are used to excite the sample. The time delay between these pulses (t_1) is scanned to generate the pump frequency axis by numerical Fourier Transformation. Following a waiting time t_2, a third pulse (probe) interacts with the sample and is sent to a grating spectrometer. The spectrum of the probe is measured directly on the frequency domain and is used to generate the vertical probe axis in the 2D IR spectrum.

Supplemental Reference

1. Oh K-I, Baiz CR. (2020). Molecular heterogeneity in aqueous cosolvent systems. The Journal of Chemical Physics.152(19):190901.

2. Schmidt-Engler JM, Blankenburg L, Blasiak B, van Wilderen L, Cho M, Bredenbeck J. (2020). Vibrational Lifetime of the SCN Protein Label in H_2O and D_2O Reports Site-Specific Solvation and Structure Changes During PYP's Photocycle. Anal Chem.92(1):1024-32.

3. Lee H, Choi JH, Cho M. (2010). Vibrational solvatochromism and electrochromism of cyanide, thiocyanate, and azide anions in water. Phys Chem Chem Phys.12(39):12658-69.